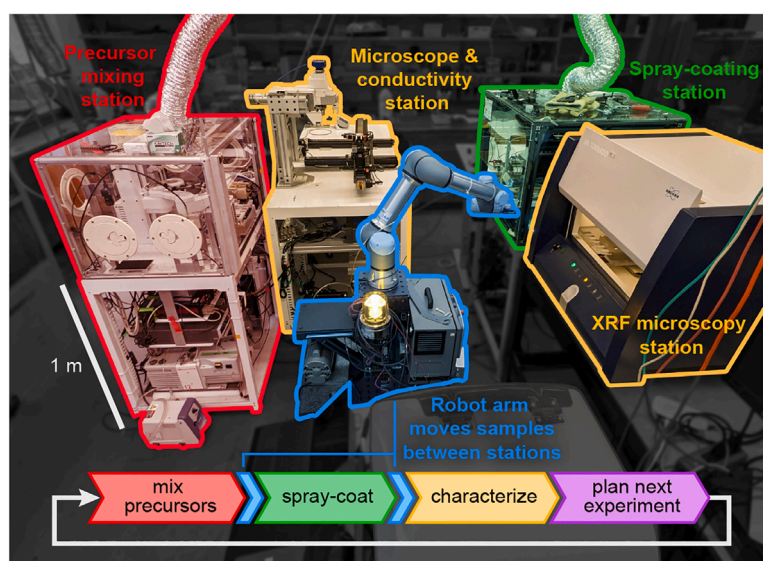


Article

A self-driving laboratory optimizes a scalable process for making functional coatings



Connor C. Rupnow, Benjamin P. MacLeod, Mehrdad Mokhtari, ..., Elija I. de Hoog, Abhishek Soni, Curtis P. Berlinguette

cberling@chem.ubc.ca

Highlights

Self-driving lab with spray-coating capabilities

Optimization of highly conductive solution-deposited palladium thin films

Scale-up of spray-coated films 8× with no loss in conductivity

Gained insights into the complex processes involved in spray coating

Rupnow et al. use a self-driving laboratory to optimize a scalable spray-coating process for producing conductive palladium films. The best coatings exhibit conductivities comparable with vacuum-sputtered coatings. The optimized process was successfully scaled to an 8× larger area. This work demonstrates the potential of self-driving laboratories to accelerate the commercialization of materials.

Rupnow et al., Cell Reports Physical Science 4, 101411
May 17, 2023 © 2023 The Author(s).
<https://doi.org/10.1016/j.xcrp.2023.101411>



Article

A self-driving laboratory optimizes a scalable process for making functional coatings

Connor C. Rupnow,^{1,2,3} Benjamin P. MacLeod,^{2,3} Mehrdad Mokhtari,² Karry Ocean,² Kevan E. Dettelbach,² Daniel Lin,² Fraser G.L. Parlane,^{2,3} Hsi N. Chiu,² Michael B. Rooney,² Chris E.B. Waizenegger,² Elija I. de Hoog,² Abhishek Soni,² and Curtis P. Berlinguette^{1,2,3,4,5,6,*}

SUMMARY

Functional coatings are used in a wide range of high surface-area technologies, such as low-E windows and photovoltaics. Solution-based coatings are typically less expensive to produce than vacuum-based coatings; however, it is generally more difficult to produce high-quality coatings using solution-based methods due to lower control over the physical and chemical processes involved. Here, we show how a self-driving laboratory can be used to optimize spray coating parameters. For this demonstration, we optimized the combustion synthesis of spray-cast conductive palladium (Pd) films. The closed-loop optimization yielded films with conductivities of >4 MS/m, which compares favorably with the conductivities of 2–6 MS/m reported for thin Pd films obtained by vacuum-based sputtering processes. The champion coating conditions were scaled up to an $8\times$ larger area using the same spray-coating apparatus while preserving coating quality and conductivity. This work shows how self-driving laboratories can optimize solution-based coatings at scale.

INTRODUCTION

Coatings are essential for manufacturing clean energy technologies such as photovoltaics,¹ electrochromics,² and electrolyzers.³ Methods for depositing coatings at scale include vacuum-based (e.g., sputtering, thermal evaporation) and solution-based (e.g., blade coating, inkjet printing, spray coating) techniques. Solution-based coating methods that avoid vacuum offer an opportunity to lower the cost and energy utilization of manufacturing clean energy technologies.^{4,5}

It is often challenging, however, to obtain performant and defect-free coatings on large areas using solution-based methods.^{6,7} These methods involve a complex interplay between wetting phenomena,⁸ solvent evaporation,⁹ solidification processes,^{10,11} and, in some cases, chemical reaction kinetics.¹² Moreover, the processes commonly used to study solution-based coatings in the laboratory (e.g., spin coating, drop casting) typically do not translate to large-scale manufacturing. While spray coating is effective for coating small substrates for exploratory materials research, it remains challenging to optimize because of the number of experimental variables and objectives^{13–15} (Figure S1).

Self-driving laboratories (SDLs) present an opportunity to accelerate the development of spray-coating processes suitable for large-scale, low-cost manufacturing of clean energy technologies. An SDL consists of an automated experiment controlled by an experiment-planning algorithm. These autonomous laboratories use data from completed

¹Department of Chemical & Biological Engineering, The University of British Columbia, 2360 East Mall, Vancouver, BC V6T 1Z3, Canada

²Department of Chemistry, The University of British Columbia, 2036 Main Mall, Vancouver, BC V6T 1Z1, Canada

³Stewart Blusson Quantum Matter Institute, The University of British Columbia, 2355 East Mall, Vancouver, BC V6T 1Z4, Canada

⁴Canadian Institute for Advanced Research (CIFAR), MaRS Centre, West Tower, 661 University Avenue Suite 505, Toronto, ON M5G 1M1, Canada

⁵Twitter: @cpbCleanEnergy

⁶Lead contact

*Correspondence: cberling@chem.ubc.ca
<https://doi.org/10.1016/j.xcrp.2023.101411>



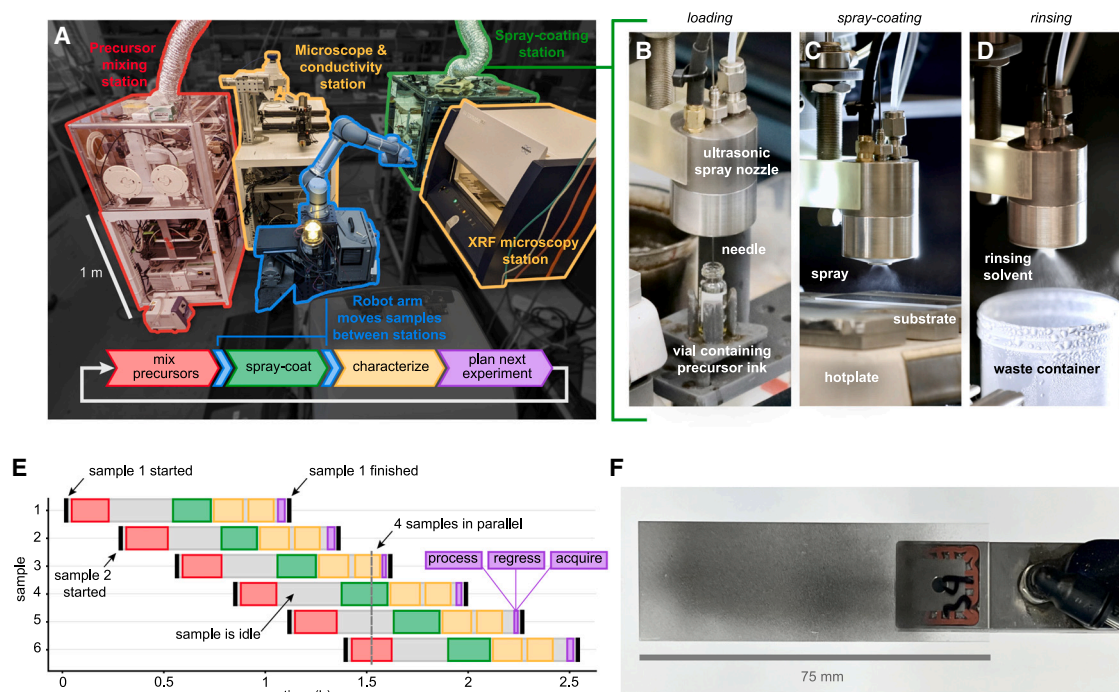


Figure 1. Ada, an SDL designed to optimize scalable spray-coating processes

(A) The SDL consists of two synthesis and two characterization stations linked together by a central six-axis robotic arm. The robotic arm transports spray-coating precursor inks in 2-mL vials (B) and thin-film samples on 75 × 25-mm glass substrates (F) between stations as required to execute the parallelized closed-loop optimization workflow shown in simplified serial form in (A, inset) and in full detail in (E).

(B–D) The spray-coating station is custom designed to load precursor inks through a retractable needle that protrudes through the nozzle (B). Front loading minimizes the volume of precursor ink required to prime the nozzle. This enables small volumes (<1 mL) of precursor ink to be sprayed without wasting ink. The loaded precursor ink is sprayed on to a heated substrate to form a coating. (C). When spraying is complete, a solvent rinse is automatically performed to clear the nozzle of residual precursor ink (D).

(E) A timeline of the parallelized workflow used for the optimization campaign. Ada's station architecture setup enables Ada to work on up to four samples in parallel. This parallel workflow enables around four experiments per hour and up to 100 spray-coating experiments per day. For clarity, the durations of the brief (<1 min) experiment-planning steps (purple) are not shown to scale. The experiment-planning process consists of three steps: data processing, GP regression, and acquisition of new experimental conditions.

(F) The Pd film sample (left) is moved between stations by the six-axis robotic arm using a vacuum handler (right).

experiments to algorithmically plan future experiments. This data-driven approach to experiment planning enables SDLs to optimize material properties and synthesis procedures up to 100× faster than automation alone.^{16,17} While numerous SDLs have implemented lab-scale solution-based coating methods,^{17–21} an SDL for optimizing large-scale solution-based coating processes has not yet been reported.

Conductive palladium (Pd) coatings have applications in fuel cells,²² CO₂ utilization,²³ and electrochemical hydrogenation.^{24,25} A technique known as spray-combustion synthesis can be used to cast Pd films from solution.^{12,17,26,27} These spray-coated Pd films have had reported conductivities of up to 2 MS/m¹⁷, which only barely reaches the 2- to 6-MS/m range of sputtered films.^{28,29} Here, we built Ada, the first SDL with spray-coating capabilities and used it to optimize a spray-coating deposition process for highly conductive Pd thin films (Figure 1). We demonstrate the power of this platform by using it to maximize the conductivity of spray-coated Pd films by manipulating seven input variables simultaneously. The experimental data generated by the SDL allowed us to identify explanations for the optimal process conditions. Moreover, we were able to scale up our results by using the identified champion Pd film recipe to produce a film 8× larger with no loss in conductivity.

RESULTS

Upgrade of SDL

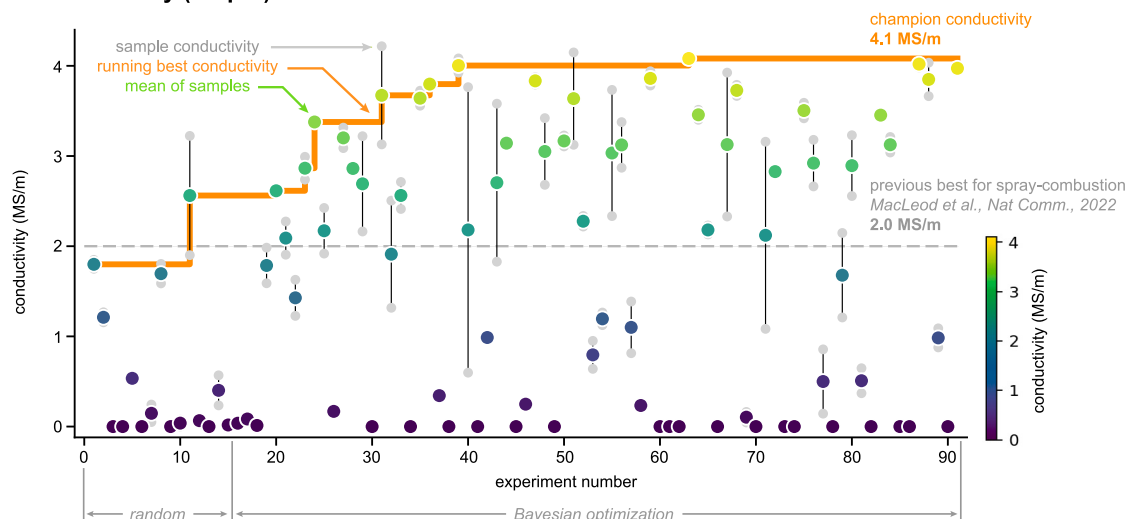
To autonomously optimize the spray-coating process, we leveraged flexible automation³⁰ to substantially upgrade our existing SDL,^{17,18} “Ada,” with improved software architecture and two new modules: a characterization station for microscope images and conductivity measurements, and a purpose-built ultrasonic spray coater (see Figures 1A–1D, and section “experimental procedures”). We designed the spray coater to enable rapid, automated spray-coating experiments. Ada’s upgraded software architecture enables parallelized workflow (Figure 1E) to perform up to 100 spray-coating experiments per day without human intervention. Ada iteratively optimizes the spray-coating process and precursor ink composition under the control of a Bayesian optimization algorithm³¹ (see inset to Figure 1A and experimental procedures).

Overview of autonomous workflow

Ada optimized the Pd film conductivity in a closed loop by autonomously performing 91 cycles of precursor preparation, spray coating, film characterization, and algorithmic experiment planning (see Figure 1A inset). In each cycle, a unique experimental condition was tested in duplicate (except for three rare instances where duplicates were missed due to system failures). Each experimental cycle involved seven steps, all of which were performed autonomously by Ada (see section “experimental procedures,” autonomous workflow steps 1–7). Ada began each experimental cycle by requesting an experimental condition to test from an experimental planning algorithm. To initialize this algorithm, the first 15 experimental conditions were chosen at random from a uniform random distribution over the input space (step 1). The precursor mixing station then prepared ~0.38 mL of spray-coating precursor ink in a 2-mL vial (step 2). The precursor ink vial and a clean 25 × 75-mm glass substrate were then transported from the precursor mixing station to the spray-coating station by the central robotic arm. The precursor ink was then sprayed onto a pre-heated glass substrate to form an approximately 10- to 100-nm-thick Pd coating (step 3). With the sample synthesis complete, the robotic arm then picked up the completed sample and passed it to the automated characterization stations. The Pd coating thickness was measured by X-ray fluorescence (XRF) microscopy (step 4). Each film was imaged using an optical microscope and the coating conductance was measured with a four-point probe (step 5). The Pd coating sample was then returned to the storage rack. The coating conductivity was calculated using conductance and thickness measurements (step 6). To complete each cycle, the experimental data generated (i.e., the experimental conditions tested and the resulting coating conductivity) were processed and fed into a single-objective Bayesian optimizer. The optimizer selected the next experimental condition to test using all the data available from previously completed samples (step 7). The full workflow of the SDL is shown in Video S1.

To maximize experimental throughput, Ada was configured so that all hardware stations operated on different samples in parallel. This configuration enabled the system to work on up to four samples at any one time (see Figure 1E). This parallelization scheme increased experimental throughput by 300% but required the experiment-planning algorithm to plan new experiments while the last three requested samples were not yet complete. In this situation, a conventional Bayesian optimizer designed for serial experiments repeatedly requests the same experimental conditions, a potentially undesirable behavior. To avoid excessively replicating the same experimental condition, we configured the optimizer with an acquisition function that

A conductivity (output)



B experimental conditions (inputs)

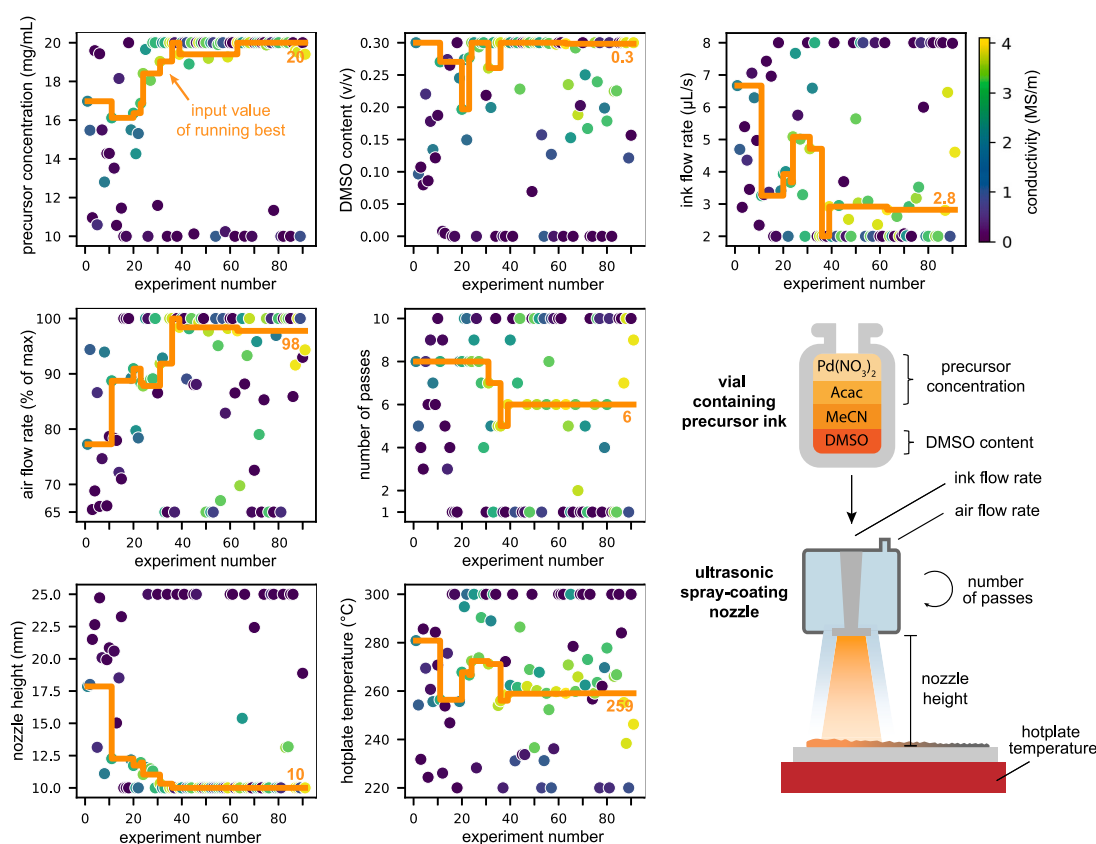


Figure 2. Autonomous optimization of the conductivity of a spray-coated Pd film

(A) Bayesian optimization was performed over 91 experiments. Each experiment was performed in duplicate (except for three rare instances where duplicates were missed due to system failures) and a maximum mean conductivity of 4.1 MS/m was achieved, more than double the best previously reported conductivity for spray combustion.¹⁷ The orange line represents the running best conductivity over time.

(B) Seven input variables were manipulated: two ink composition variables (DMSO content and solute concentration) and five spray-coating variables (ink flow rate, airflow rate, number of passes, height, and hotplate temperature). The experimental conditions requested for each

Figure 2. Continued

experiment are shown in each plot. The bounds of the experimental variables are shown as the minimum and maximum y axis value for each plot (see also Table S1 and Note S3). The orange line represents the input values associated with the running best conductivity. The input value yielding the champion Pd film is shown at the end of each orange line.

alternated between four modes. The first three modes used the upper confidence bound acquisition function with $\beta = 0.25$, 25, and 400, respectively (see [supplemental experimental procedures](#)). The fourth mode selected a space-filling point (i.e., the furthest point from any previously tested point in the input space, see section “space-filling point” in the “[experimental procedures](#)”), as suggested by Schmidt et al.³² This four-mode acquisition function balances exploitation and exploration, avoids suggesting replicate samples, and ensures robust explorative behavior by choosing space-filling points in a way that does not depend on the quality of the surrogate model (see Figure S2 and [supplemental experimental procedures](#)). Further details of the optimizer configuration are provided in the section “experimental procedures” (see autonomous workflow step 7).

Maximization of Pd film conductivity

We configured Ada to autonomously maximize the Pd film conductivity by manipulating seven experimental variables (precursor concentration, dimethyl sulfoxide [DMSO] content, ink flow rate, airflow rate, number of passes, nozzle height, hotplate temperature) that control the spray-coating process (Figure 2, Table S1). Each manipulated variable was chosen according to a hypothesis. Hotplate temperature was varied because higher synthesis temperatures are known to improve charge transport in combustion-synthesized films.^{12,17} Precursor concentration was varied because it influences overall film thickness, which can influence conductivity through percolation and boundary scattering effects.^{28,33} The number of spray-coating passes was varied because it influences the thickness of the reacting precursor layer, which is known to control film porosity in combustion-synthesized films and may thus affect conductivity.¹² Spray nozzle height, precursor ink flow rate, and airflow rate were varied because these variables are known to affect the roughness of spray-coated films,¹³ and roughness tends to decrease film conductivity.³⁴ DMSO content was varied because our initial observations (see Figure S3) and literature data both showed that adding a co-solvent with a high boiling point can increase the temperature at which coatings can be deposited by spraying.³⁵ The ranges of values over which each variable was manipulated were chosen based on prior knowledge of conditions known to produce films with measurable conductivity or based on physical limitations (e.g., maximum solubility, equipment limits). The variable ranges are shown as the minimum and maximum y value of each axis in Figure 2B.

The results of the optimization are shown in Figure 2. The experimental condition yielding the highest mean conductivity across duplicates was identified after 63 cycles of experimentation (Figure 2A). This champion experiment with a conductivity of 4.1 MS/m doubles the best previously reported value of 2.0 MS/m for Pd films deposited by spray combustion¹⁷ and is comparable with the conductivities of sputtered films, which range from 2 to 6 MS/m.^{28,29} The relative conductivity difference between the duplicate samples created using the champion experimental conditions was less than 1% (see Note S1 for a discussion of the experimental variability and possible sources thereof).

Ada tested a large number of diverse experimental conditions over the course of the optimization campaign (Figure 2B). These rich data provide insights about the Pd

spray-combustion process beyond the simple identification of conditions that maximize film conductivity. We were able to identify explanations for the optimal spray-coating conditions that are supported by data from the optimization campaign, follow-up experiments, and the literature.

Ada identified a high precursor concentration (20 mg/mL) as optimal (see [Figure 2B](#), precursor concentration). The data revealed that the film conductivity was strongly correlated with thickness (see [Figure S4](#)). We attribute this observation to the gradual percolation of conductive Pd islands as the film thickness increases, as has been observed, for example, with nanogranular gold films³³ (we note that our Pd films show nano-granularity in SEM images; see [Figure S5](#)). High precursor concentration increases film thickness (and thus conductivity) by simply adding more Pd to the film (see [Figure S6](#)). Ada found that the lowest allowed nozzle height (10 mm) was optimal (see [Figure 2B](#), nozzle height). Low nozzle height increases film thickness (and thus conductivity) by reducing overspray and thus depositing a larger fraction of the precursor onto the substrate (see [Figure S6](#)).

The optimal values for the remaining input parameters appear to arise due to a complex interplay between the film thickness, the precursor composition, the spray-coating conditions, the local substrate temperature, and the Leidenfrost effect. The Leidenfrost effect occurs when a droplet of a liquid impinging on a hot surface becomes suspended on a cushion of its own vapor. This effect is known to slow or prevent film deposition of spray-coated materials at high temperatures by repelling precursor droplets from the heated substrate.³⁵ Fluid phenomena such as the Leidenfrost effect create complex relationships between coating conditions and outcomes. This complexity can make it difficult to transfer knowledge from one coating method to another (e.g., from drop casting to spray coating as found here).

Ada identified an intermediate temperature (259°C) as optimal (see [Figure 2B](#), hot-plate temperature). This optimum appears to avoid the detrimental Leidenfrost effect that occurs at higher temperatures while providing sufficient thermal energy to drive the combustion of the precursor.^{17,27} Ada found that adding large amounts of DMSO (30% v/v) into the precursor ink maximized the conductivity (see [Figure 2B](#), DMSO content). The beneficial effect of DMSO appears to arise from the suppression of the Leidenfrost effect. The suppression of the Leidenfrost effect occurs from the higher boiling point of DMSO ($T_{\text{vap}} = 189^\circ\text{C}$) compared with the other solvent used in our precursor inks (acetonitrile, $T_{\text{vap}} = 82^\circ\text{C}$) ([Figure S7](#)). To support this conclusion, we used Ada to perform a series of follow-up experiments that show that inks containing DMSO result in thicker Pd films at higher temperatures ([Figure S8](#)).

Ada found that a high flow rate of air from the nozzle (control valve opened to 98% of the maximum) was optimal (see [Figure 2B](#), airflow rate). We attribute this to suppression of the Leidenfrost effect caused by transient cooling of the substrate by this impinging airflow. Transient cooling enables the precursor to efficiently coat the substrate by avoiding the Leidenfrost effect, while subsequent reheating of the substrate promotes the complete transformation of the precursor into metallic Pd. Thermography and thermocouple data show that the nozzle causes rapid transient cooling and reheating of the substrates in our system, with temperature swings as large as 30°C (see [Figure S9](#)). Stronger transient cooling of the substrate may also be an additional benefit of low nozzle height. Ada found that low flow rate of ink from the nozzle (2.8 $\mu\text{L/s}$) was optimal (see [Figure 2B](#), ink flow rate). Since the ink volume sprayed was fixed, lower ink flow rates led to slower nozzle speeds. This caused the nozzle to remain over the substrate for longer, providing more time for the air from

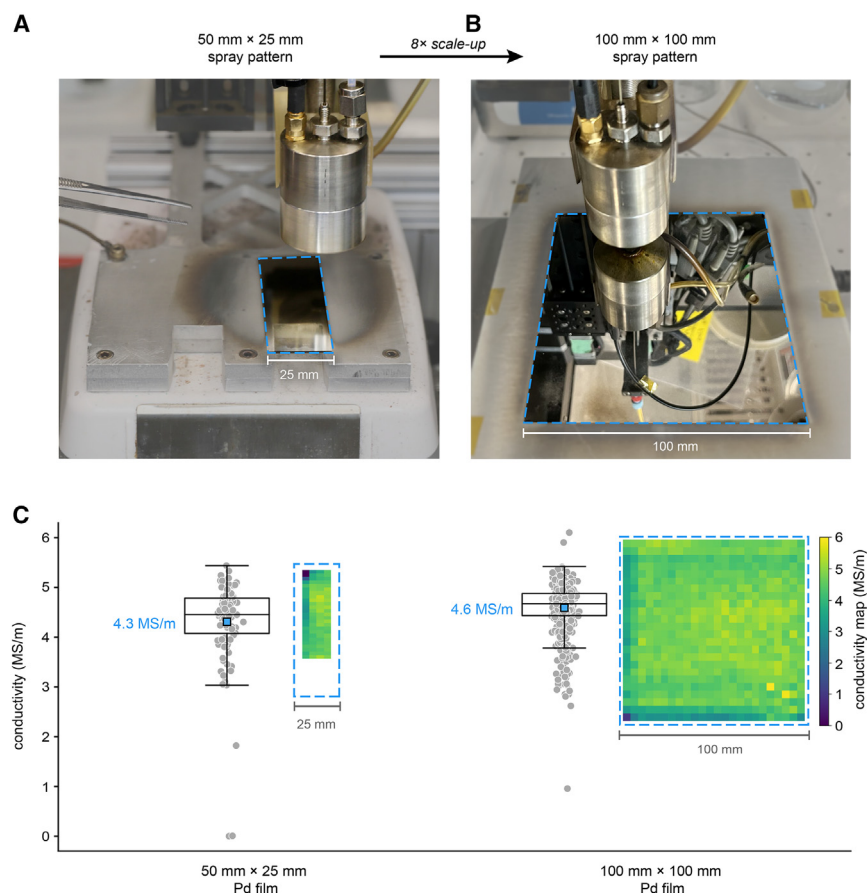


Figure 3. The identified champion coating conditions were scaled up to an 8× larger area with no further optimization and with no loss in coating conductivity

(A and B) The champion conditions identified by the optimization campaign were successfully scaled up from (A) 50 × 25 mm to (B) 100 × 100 mm, to create a coating of 8× larger area with no modifications other than the requisite increase in the size of the nozzle pattern and ink volume (see Figure S12).

(C) Conductivity was measured in a grid pattern on the small- and large-scale films (see section “scale-up of experiment” in “experimental procedures”). The conductivity of each measurement is shown in the conductivity map. The color of each pixel in the conductivity map corresponds to the y value of one of the scatter points next to it. A boxplot shows the interquartile ranges of conductivity measurements while the blue square represents the mean. A small random value was added to the x value of each scatter point (i.e., jitter) to improve visibility of the distribution of conductivity values. The larger film was slightly more conductive and uniform than the smaller film, exhibiting a conductivity of 4.6 ± 0.5 MS/m and 4.3 ± 0.9 MS/m, respectively (see Note S4).

the nozzle to locally cool the surface and further suppress the Leidenfrost effect (see Figures S9 and S10). The number of spray-coating passes appeared to be the least important manipulated variable; high-conductivity films were obtained across all settings for this variable (see Figure 2B, number of passes).

Scale-up of the champion coating conditions

Following the optimization campaign, the conditions yielding the champion Pd film were scaled up to a larger area with no further optimization and no reduction in coating quality (Figure 3). Specifically, we used the same champion conditions and the same spray coater used for the optimization campaign to deposit a Pd film on a 100 × 100-mm glass substrate (see section “scale-up of experiment” in “experimental procedures”). The

scaled-up spray-coating process yielded a highly reflective large-area Pd film that had a slightly higher and more uniform conductivity (4.6 ± 0.5 MS/m) than the small-scale samples autonomously optimized by Ada (4.3 ± 0.9 MS/m). The uniformity of film conductivity achieved by the spray-coating technique ($\pm 11\%$ for the large sample) was comparable with that achieved by sputtering ($\pm 8\%$; see Figure S11). We expect this spray-coating process to scale to even larger areas so long as the process conditions (e.g., substrate temperature) can be held sufficiently uniform across the substrate. Our success in scaling up the champion coating conditions using the same process conditions highlights the value of directly optimizing a scalable coating process such as spray coating using an SDL.

DISCUSSION

In this study we used an SDL to optimize a complex spray-combustion process for depositing conductive Pd coatings. The optimization campaign discovered conditions for preparing highly conductive Pd coatings (>4 MS/m) by spray coating. The optimal coating conditions identified by the SDL were comparable with conductivities exhibited by sputtered Pd films and were readily scaled up from a 1,250-mm² film to a 10,000-mm² film without compromising the conductivity. The rich data generated by the SDL also yielded insights into the complex processes at play during the spray-combustion synthesis of Pd coatings, such as how the Leidenfrost effect can detrimentally affect the spray-coating process at high substrate temperatures. This work shows how SDLs can be used to address the challenges associated with scaling up solution-based coating methods.

EXPERIMENTAL PROCEDURES

Resource availability

Lead contact

Further information and reasonable requests for resources and reagents should be directed to and will be fulfilled by the lead contact, Curtis Berlinguette (cberling@chem.ubc.ca).

Materials availability

This study did not generate new, unique reagents.

Data and code availability

The raw and processed data generated by the SDL in this study are available at <https://github.com/berlinguette/ada>. All other data related to this paper are available from the corresponding author upon request. All code used in this study was based on open-source Python packages listed in the supplemental information.

Manual preparation of stock solutions

Stock solutions were prepared by hand and stored in capped 2-mL high-performance liquid chromatography (HPLC) vials. These vials were placed in a tray that was accessible to a robotic arm of the SDL. The Pd(NO₃)₂·H₂O and acetylacetone solutions were prepared in acetonitrile (MeCN) at a concentration of 30 mg mL⁻¹. Pd(II) nitrate hydrate (Pd(NO₃)₂·H₂O; Pd ~40% m/m; 99.9% Pd purity, CAS 10102-05-3) was purchased from Strem Chemicals. MeCN (CAS 75-05-8; HPLC grade, $\geq 99.9\%$ purity) and acetylacetone (CAS 123-54-6; $\geq 99\%$ purity) were purchased from Sigma-Aldrich. All chemicals were used as received.

Manual preparation of consumables

The SDL used the following consumables as received: glass substrates (75 × 25 × 1-mm microscope slides; VWR catalog no. 16004-430); 2-mL HPLC vials (Canadian

Life Science); and 200- μ L pipettes (Biotix, M-0200-BC). These items were placed in racks and trays for access by the SDL.

Autonomous workflow step 1: Select conditions for initial experiments

A set of 15 initial random experiments were chosen to initialize the optimization. This amount was chosen based on an arbitrary $2n + 1$ rule, where n is the number of dimensions. A random value between 0 and 1 was chosen for each experimental condition from a uniform random distribution (Python `numpy.random.random`). This value was then scaled to the range of the variable. Since each experiment was performed in duplicate, 30 samples with 15 unique experimental conditions were used to initialize the optimization.

Autonomous workflow step 2: Mix precursor

A four-axis laboratory robot (N9, North Robotics) located within the precursor mixing station formulated each precursor ink by pipetting the stock solutions described above into a clean 2-mL HPLC vial. The total requested volume of the precursor ink (0.38 mL) remained fixed, while the volume of each individual stock solution within the precursor ink was allowed to vary. Each precursor ink had a requested precursor concentration ($\text{Pd}(\text{NO}_3)_2$ and acetylacetone) and DMSO content. The required amounts of $\text{Pd}(\text{NO}_3)_2$ and acetylacetone to reach the set concentration in 0.38 mL were first pipetted into the vial. MeCN and DMSO were then added to the vial up to 0.38 mL in order to reach the set concentration and DMSO content. Gravimetric feedback from an analytical balance (ZSA120, Scientech) was used to record the true (or “realized”) amount of dispensed precursor and minimize pipetting errors (see [Figure S13](#)). The vial was then placed back into a holding tray once mixing was complete.

Autonomous workflow step 3: Spray coat

A blank glass substrate (75 \times 25 \times 1-mm microscope slides; VWR catalog no. 16004-430) and a vial containing the precursor ink were passed from the precursor mixing station to the spray-coating station. Glass substrates were stored on a substrate rack at the precursor mixing station. The N9 robot used a custom vacuum chuck to pick up a substrate from the substrate rack and drop it off at a transfer tray. This transfer tray allowed the transfer of samples between the N9 robot and a six-axis robotic arm (UR5e, Universal Robotics). The UR5e picked up the substrate from the transfer tray and dropped it off at the spray-coating station. The UR5e uses a vacuum chuck affixed to the end-effector, similar to the vacuum chuck that is used by the N9. A vial containing the precursor ink was picked up by the N9 robot and passed to the spray-coating station via the UR5e arm. The vials were transferred using a custom 3D-printed vial carrier that allowed the vials to be transported with the vacuum chuck on the UR5e robot arm.

The spray coater was built from an ultrasonic nozzle (Microspray, USA) mounted to a custom motorized XYZ gantry system (Zaber Technologies, Canada) above a hotplate (PC-420D, Corning, USA). A custom aluminum fixture (alloy 6061, 12.7 mm thick) with notches for substrate access was mounted to the hotplate. This fixture enabled substrates to be picked up and set down on the hotplate by the UR5e robot arm.

Precursor ink was front loaded into the spray coater nozzle via a needle that protrudes through the center bore in the ultrasonic nozzle. A pneumatic solenoid used compressed air to control the extension and retraction of the needle. A syringe pump (cavro centris pump PN: 30098790-B, Tecan Trading AG, Switzerland) controlled the flow of precursor ink using isopropyl alcohol as a backing solvent. A

50- μL gap between the backing solvent and the precursor ink separated the two fluids in the tubing (Cole-Parmer, PTFE, 1-mm internal diameter [ID]). The ultrasonic spray nozzle was operated at 3 W and 120 kHz. For each recipe, a total of 300 μL of precursor was sprayed onto a pre-heated glass substrate.

Hotplate temperature was measured using a thermocouple mounted to the surface of the hotplate aluminum fixture. The thermocouple provided feedback to a proportional-integral-derivative (PID) controller ($k_p = 0.7$, $k_i = 3.5$, $k_d = 65$) that turned the hotplate on or off to maintain a constant surface temperature.

When spraying, the nozzle moved in a serpentine pattern consisting of 12 lines 50 mm in length and evenly spaced within the 25-mm-wide glass slide (see [Figure S12A](#)). This pattern was repeated for the requested number of passes with a 30-s delay between each pass. The spray coater nozzle speed varied between 2 and 168 mm s^{-1} , depending on the number of passes. Nozzle speed was calculated by dividing the total distance that the nozzle traveled by the amount of time the nozzle needed to spray all 300 μL at a particular flow rate.

Compressed air was fed to the nozzle at 60 PSI but was restricted by an electronic air control valve (EV-P-20-2550, Clippard, USA). This valve varied between 65% and 100% of the maximum. A valve setting of 100% was measured to be 22 standard cubic feet per hour (SCFH), while a value of 65% was measured to be 16 SCFH. The height of the nozzle above the substrate, controlled by the motorized XYZ gantry system, varied between 10 and 25 mm. The spray flow rate, controlled by the syringe pump, varied between 2 and 8 $\mu\text{L s}^{-1}$. After spray coating, the samples were left to rest on the hotplate for a minimum of 200 s.

Autonomous workflow step 4: XRF

Hyperspectral XRF images of each sample were acquired using a Bruker M4 TORNADO X-ray fluorescence microscope. Samples were transported from the spray-coating station to the XRF microscope by the UR5e robot arm. The instrument was equipped with a customized sample fixture employing an alignment tool.

The XRF microscope operated using a rhodium X-ray source at 50 kV/600 μA /30 W. The X-ray optics yielded a 25- μm spot size on the sample. The instrument achieved an energy resolution of 10 eV via twin 30- mm^2 silicon drift detectors. Hyperspectral images were taken over a 16 \times 16-mm area at a resolution of 40 \times 40 pixels. The XRF spectra obtained (reported in counts) were scaled by the integration time (200 m) and the energy resolution (10 eV) to yield units of counts $\text{s}^{-1} \text{eV}^{-1}$.

To quantify the relative amount of Pd in the film, the XRF spectra were integrated at the Pd Lyman-alpha X-ray fluorescence line (2.837 keV) from 2.6 to 3.2 keV. The resulting counts were converted to film thickness estimates by applying a calibration factor obtained using reference samples (see below). Five points of interest were defined within the XRF hypermap of the sample, spaced 2 mm apart vertically down the center of the XRF hypermap (see [Figure S12A](#)). For each point of interest, the XRF counts per second were averaged over a 3 \times 3-mm area.

Calibration of XRF signal against reference samples

To enable Pd film thickness to be estimated from the XRF signal, a calibration procedure was performed according to MacLeod et al.¹⁷ Sputtered Pd reference samples were fabricated having four different nominal thicknesses (10, 50, 100, and 250 nm). These samples were characterized by profilometry and XRF. A linear

relationship between the film thickness and the XRF counts was observed with a slope of $3.658 \times 10^{-4} \text{ nm cps}^{-1}$ and intercept of -27.25 nm . This relationship was used to estimate the thickness of each sample from the XRF data.

Autonomous workflow step 5: Conductivity and imaging

After XRF imaging, the UR5e robot transported the Pd film sample to the microscope and conductivity station. This station consists of a four-point conductivity probe and optical microscope that is serviced by a six-degrees-of-freedom gantry robot composed of motor stages from Zaber Technologies. A custom end-effector mounted on the motor stack is used to secure samples in place during characterization using spring-loaded tabs.

The samples were imaged using an Axio Imager Vario.Z2 microscope from Zeiss. Brightfield and darkfield images were captured at $2.5\times$ and $20\times$ magnification at 2 mm above and below the center of the film. Focus and exposure parameters for each sample were determined with an automatic routine through Zen Blue software provided by Zeiss.

Following optical microscopy, the gantry moved the sample to the four-point probe. Four-point probe conductance measurements were acquired using a Keithley Series K2636B System Source Meter instrument connected to a Signatone four-point probe head (part number SP4-40045TBN; 0.040-inch tip spacing, 45-g pressure, and tungsten carbide tips with 0.010-inch radii) by a Signatone triax to BNC feedthrough panel (part number TXBA-M160-M). The source current was stepped from 0 to 1 mA in 0.2-mA steps. After each current step, the source meter was stabilized for 0.1 s and the voltage across the inner probes was then averaged for three cycles of the 60-Hz power line (i.e., for 0.05 s) and recorded. Conductance measurements were made on the same five points of interest as analyzed in the XRF data (see Figure S12A).

The samples were then positioned 30 cm below an optical camera (FLIR Blackfly S USB3; BFS-U3-120S4C-CS) using a Sony 12.00 MP CMOS sensor (IMX226) and an Edmund Optics 25 mm/f1.4 C-Series Fixed Focal Length Imaging Lens (#59-871) for imaging. White printer paper was placed 2.5 cm behind the sample to improve image contrast.

Autonomous workflow step 6: Process the raw data

The film conductivity was calculated using a custom data analysis pipeline implemented in Python using the open-source Luigi framework.³⁶ This pipeline combined conductance data and XRF data to estimate the film conductivity at each of the five points of interest on the sample.

For each set of current-voltage measurements at each position on each sample, a linear fitting algorithm was used to extract the conductance (dI/dV). The voltage compliance limit of the K2636B was set to 10 V and voltage measurements greater than 10 V were therefore considered to have saturated the source meter instrument and were automatically discarded by the data analysis pipeline.

The conductivity of the thin films was then calculated by combining the four-point-probe conductance data with the film thicknesses estimated by XRF:

$$\sigma = \frac{\ln 2}{\pi} \left(\frac{dI}{dV} \right) t^{-1} \quad (\text{Equation 1})$$

where dI/dV is the conductance from the four-point-probe measurement, t is estimated film thickness from the XRF measurements, and σ is conductivity.

Outliers were excluded from the conductance data using a kernel density exclusion method (see below). Outliers were also excluded from the XRF film thickness estimates using the same exclusion method. Conductivities were calculated for each position on the sample for which neither conductance nor XRF data were excluded. The mean of these conductivities was returned to the optimizer (see below). In cases where all points were discarded, a mean conductivity of 0 was reported.

The outlier kernel density exclusion method was performed by calculating Gaussian kernel density estimates for the conductance and XRF data, normalizing the density between 0 and 1, and rejecting data points with a kernel density below 0.3. Bandwidths of $5 \times 10^{-3} \mu\Omega^{-1} \text{ m}^{-1}$ and $5 \times 10^3 \text{ cps}$ were used for the conductance and XRF data, respectively.

Autonomous workflow step 7: Choose the next experiment

To choose the next experiment, Ada requested a new set of experimental conditions from a queue. If there was a sample in the queue, then Ada made and tested that sample. If the queue was empty, a new set of experimental conditions were requested from the optimizer. Following the 15 random experiments (described in step 1), the optimizer was configured to pass experiments to the queue that were selected using Bayesian optimization.

The Bayesian optimization was performed using the Botorch Python package³¹ and happened in two steps. First, a surrogate Gaussian process (GP) regression model was built over all existing data. The data covariates were normalized to the unit cube and outcomes were standardized (zero mean, unit variance). A fixed-noise GP model was used for the surrogate model with standard deviation of the input data estimated to be of 0.2 MS/m. We chose 0.2 MS/m as the noise estimate because it is 10% of the previously reported maximum conductivity value for this technique. All other hyperparameters for the GP model were default. The model predictions are discussed in [Note S2](#) and in [Figures S14–S17](#).

Second, an acquisition function was selected and a new set of experimental conditions were acquired. The acquisition function cycled between four modes; upper confidence bound (UCB) with three different beta values (beta of 0.25, 25, 400) and a space-filling point. The space-filling point selected an experimental condition in the parameter space that maximized the distance to the closest other existing experiment. This cycling was necessary to accommodate our parallel workflow. The acquisition functions were configured to maximize the conductivity while also effectively searching the parameter space. Once a set of experimental conditions were found (via UCB or space filling), the optimizer would duplicate the result and pass two sets of experimental conditions to the queue.

This autonomous workflow from steps 2 to 7 was repeated until a critical error ultimately stopped the optimization after 91 experiments. During the optimization, the SDL was stopped briefly four times to refill consumables or to adjust a hardware component. Occasionally, these stops resulted in some experimental conditions not having a duplicate (e.g., experiments 44, 46, 91). Re-booting the SDL after a brief stop occasionally resulted in the same acquisition function being used twice (or more) in a row (e.g., experiments 16/17 and 60/61).

Space-filling point

The space-filling point algorithm employed a Monte-Carlo-based distance optimization. A selection of 100 random points were chosen in the parameter space.

Each point was individually optimized according to a scheme that maximized the objective function, $\min(\|x - a\|^2)$, where x is the random point and a is a set of all available data points, subject to the parameter bounds (see Table S1). The `scipy.optimize.minimize` function was used to accomplish this maximization for each random point. This moves each point to the closest local maximum. The point that had the greatest objective function value (i.e., the point that was furthest away from the next closest point) was chosen as the next experiment to perform.

Scale-up of experiment

Pd precursor ink was sprayed on a 100 × 100 × 1.6-mm piece of glass. A new, larger aluminum fixture (of the same thickness) was made for the hotplate to accommodate the larger piece of glass. The scaled-up experiment used the same hotplate and thermocouple setup as was used during the optimization. The volume of ink sprayed and the spray pattern were scaled up while the experimental conditions remained the same as the optimization champion. The amount of ink sprayed increased from 0.3 to 2.4 mL and the pattern size increased from 25 × 50 mm with 12 evenly spaced lines to 100 × 100 mm with 48 evenly spaced lines (see pattern in Figure S12B). The nozzle speed remained at 33.86 mm s⁻¹ for both small and large spray patterns.

A small-scale sample from the champion experiment (sample 123 from experiment 61) was chosen to analyze for comparison against the large-scale sample. Conductance measurements were acquired with the four-point probe in a grid pattern on both samples. The small sample had a grid of 100 points extending five points spaced 4 mm apart in the x direction and 20 points spaced 2 mm apart in the y direction. The large sample had a grid of 576 points extending 24 points spaced 4 mm apart in the x direction and 24 points spaced 4 mm apart in the y direction. The samples were then both characterized for thickness. For the small sample, a high-resolution grid of XRF measurements was taken with each pixel spaced 0.2 mm apart and an integration time of 200 ms per pixel. For the large sample, a high-resolution grid of XRF measurements was taken with each pixel spaced 0.18 mm apart and an integration time of 200 ms per pixel. The high-resolution grid was down-sampled to match the pixel size and location of the conductance grid by averaging the high-resolution pixels in the bounding box of the conductance pixel size. The down-sampled XRF pixel map was converted to thickness using the same calibration curve as used during the optimization (see autonomous workflow step 4, calibration of XRF signal). The conductivity was calculated for each pixel using the same method as used during the optimization (see autonomous workflow step 6).

SUPPLEMENTAL INFORMATION

Supplemental information can be found online at <https://doi.org/10.1016/j.xcrp.2023.101411>.

ACKNOWLEDGMENTS

Funding: the authors are grateful to Natural Resources Canada's Energy Innovation Program (EIP2-MAT-001), the Canadian Natural Science and Engineering Research Council (RGPIN-2018-06748), Canadian Foundation for Innovation (229288), Canadian Institute for Advanced Research (BSE-BERL-162173), and Canada Research Chairs for financial support. The authors are also thankful to O.R. Horner and E. Ilic for their assistance in this work.

AUTHOR CONTRIBUTIONS

C.P.B. conceived and supervised the project. C.C.R., B.P.M., K.O., K.E.D., D.L., H.N.C., M.B.R., C.E.B.W., and E.I.H. developed the robotic hardware. C.C.R., M.M., K.E.D., D.L., and H.N.C. developed the robotic control software with input from B.P.M. and F.G.L.P. C.C.R. and M.M. developed the optimization algorithm with input from B.P.M. and F.G.L.P. C.C.R. designed and performed the robotic optimization experiments with assistance from M.M., A.S., and K.E.D. C.C.R., B.P.M., A.S., and M.M. performed the data analysis. C.C.R. performed additional experiments. C.C.R. and F.G.L.P. made the figures with input from B.P.M. and C.P.B. C.C.R., B.P.M., M.M., A.S., and C.P.B. contributed to writing the manuscript.

DECLARATION OF INTERESTS

The authors declare no competing interests.

Received: January 11, 2023

Revised: March 31, 2023

Accepted: April 17, 2023

Published: May 8, 2023

REFERENCES

- Yan, J., Savenije, T.J., Mazzarella, L., and Isabella, O. (2022). Progress and challenges on scaling up of perovskite solar cell technology. *Sustain. Energy Fuels* 6, 243–266.
- Cai, G., Wang, J., and Lee, P.S. (2016). Next-generation multifunctional electrochromic devices. *Acc. Chem. Res.* 49, 1469–1476.
- Zheng, T., Jiang, K., Ta, N., Hu, Y., Zeng, J., Liu, J., and Wang, H. (2019). Large-scale and highly selective CO₂ electrocatalytic reduction on nickel single-atom catalyst. *Joule* 3, 265–278.
- Smith, R.D.L., Prévot, M.S., Fagan, R.D., Zhang, Z., Sedach, P.A., Siu, M.K.J., Trudel, S., and Berlinguette, C.P. (2013). Photochemical route for accessing amorphous metal oxide materials for water oxidation catalysis. *Science* 340, 60–63.
- Cheng, W., Moreno-Gonzalez, M., Hu, K., Krzyszkowski, C., Dvorak, D.J., Weekes, D.M., Tam, B., and Berlinguette, C.P. (2018). Solution-deposited solid-state electrochromic windows. *iScience* 10, 80–86.
- Mitzi, D. (2008). *Solution Processing of Inorganic Materials* (John Wiley & Sons).
- Taherimaksousi, N., MacLeod, B.P., Parlane, F.G.L., Morrissey, T.D., Booker, E.P., Dettelbach, K.E., and Berlinguette, C.P. (2020). Quantifying defects in thin films using machine vision. *npj Comput. Mater.* 6, 111–116.
- Wang, J.Z., Zheng, Z.H., Li, H.W., Huck, W.T.S., and Siringhaus, H. (2004). Dewatering of conducting polymer inkjet droplets on patterned surfaces. *Nat. Mater.* 3, 171–176.
- Chen, B.T. (1983). Investigation of the solvent-evaporation effect on spin coating of thin films. *Polym. Eng. Sci.* 23, 399–403.
- Bretos, I., Diodati, S., Jiménez, R., Tajoli, F., Ricote, J., Bragaggia, G., Franca, M., Calzada, M.L., and Gross, S. (2020). Low-temperature solution crystallization of nanostructured oxides and thin films. *Chemistry* 26, 9157–9179.
- Virkar, A.A., Mannsfeld, S., Bao, Z., and Stingelin, N. (2010). Organic semiconductor growth and morphology considerations for organic thin-film transistors. *Adv. Mater.* 22, 3857–3875.
- Kim, M.-G., Kanatzidis, M.G., Facchetti, A., and Marks, T.J. (2011). Low-temperature fabrication of high-performance metal oxide thin-film electronics via combustion processing. *Nat. Mater.* 10, 382–388.
- Bose, S., Keller, S.S., Alstrøm, T.S., Boisen, A., and Almdal, K. (2013). Process optimization of ultrasonic spray coating of polymer films. *Langmuir* 29, 6911–6919.
- Liu, Z., Rolston, N., Flick, A.C., Colburn, T.W., Ren, Z., Dauskardt, R.H., and Buonassisi, T. (2022). Machine learning with knowledge constraints for process optimization of open-air perovskite solar cell manufacturing. *Joule* 6, 834–849.
- Schneider, A., Traut, N., and Hamburger, M. (2014). Analysis and optimization of relevant parameters of blade coating and gravure printing processes for the fabrication of highly efficient organic solar cells. *Sol. Energy Mater. Sol. Cells* 126, 149–154.
- Ament, S., Amsler, M., Sutherland, D.R., Chang, M.-C., Guevarra, D., Connolly, A.B., Gregoire, J.M., Thompson, M.O., Gomes, C.P., and van Dover, R.B. (2021). Autonomous materials synthesis via hierarchical active learning of nonequilibrium phase diagrams. *Sci. Adv.* 7, eabg4930.
- MacLeod, B.P., Parlane, F.G.L., Rupnow, C.C., Dettelbach, K.E., Elliott, M.S., Morrissey, T.D., Haley, T.H., Proskurin, O., Rooney, M.B., Taherimaksousi, N., et al. (2022). A self-driving laboratory advances the Pareto front for material properties. *Nat. Commun.* 13, 995.
- MacLeod, B.P., Parlane, F.G.L., Morrissey, T.D., Häse, F., Roch, L.M., Dettelbach, K.E., Moreira, R., Yunker, L.P.E., Rooney, M.B., Deeth, J.R., et al. (2020). Self-driving laboratory for accelerated discovery of thin-film materials. *Sci. Adv.* 6, eaaz8867.
- Langner, S., Häse, F., Perea, J.D., Stubhan, T., Hauch, J., Roch, L.M., Heumueller, T., Aspuru-Guzik, A., and Brabec, C.J. (2020). Beyond ternary OPV: high-throughput experimentation and self-driving laboratories optimize multicomponent systems. *Adv. Mater.* 32, e1907801.
- Bash, D., Cai, Y., Chellappan, V., Wong, S.L., Yang, X., Kumar, P., Tan, J.D., Abutaha, A., Cheng, J.J., Lim, Y.-F., et al. (2021). Multi-fidelity high-throughput optimization of electrical conductivity in P3HT-CNT composites. *Adv. Funct. Mater.* 31, 2102606.
- Li, Z., Najeeb, M.A., Alves, L., Sherman, A.Z., Shekar, V., Cruz Parrilla, P., Pendleton, I.M., Wang, W., Nega, P.W., Zeller, M., et al. (2020). Robot-Accelerated perovskite investigation and discovery. *Chem. Mater.* 32, 5650–5663.
- Park, J.S., Choi, H.J., Han, G.D., Koo, J., Kang, E.H., Kim, D.H., Bae, K., and Shim, J.H. (2021). High-performance protonic ceramic fuel cells with a PrBa_{0.5}Sr_{0.5}Co_{1.5}Fe_{0.5}O_{5+δ} cathode with palladium-rich interface coating. *J. Power Sources* 482, 229043.
- Gao, D., Zhou, H., Cai, F., Wang, J., Wang, G., and Bao, X. (2018). Pd-containing nanostructures for electrochemical CO₂ reduction reaction. *ACS Catal.* 8, 1510–1519.
- Sherbo, R.S., Kurimoto, A., Brown, C.M., and Berlinguette, C.P. (2019). Efficient electrocatalytic hydrogenation with a palladium membrane reactor. *J. Am. Chem. Soc.* 141, 7815–7821.
- Delima, R.S., Sherbo, R.S., Dvorak, D.J., Kurimoto, A., and Berlinguette, C.P. (2019). Supported palladium membrane reactor

- architecture for electrocatalytic hydrogenation. *J. Mater. Chem. A Mater.* **7**, 26586–26595.
26. Yu, X., Smith, J., Zhou, N., Zeng, L., Guo, P., Xia, Y., Alvarez, A., Aghion, S., Lin, H., Yu, J., et al. (2015). Spray-combustion synthesis: efficient solution route to high-performance oxide transistors. *Proc. Natl. Acad. Sci. USA* **112**, 3217–3222.
27. Voskanyan, A.A., Li, C.-Y.V., and Chan, K.-Y. (2017). Catalytic palladium film deposited by scalable low-temperature aqueous combustion. *ACS Appl. Mater. Interfaces* **9**, 33298–33307.
28. Shi, Y.S. (2003). Electrical resistivity of RF sputtered Pd films. *Phys. Lett.* **319**, 555–559.
29. Anton, R., Häupl, K., Rudolf, P., and Wißmann, P. (1986). Electrical and structural properties of thin palladium films. *Z. Naturforsch.* **41**, 665–670.
30. MacLeod, B.P., Parlane, F.G.L., Brown, A.K., Hein, J.E., and Berlinguette, C.P. (2022). Flexible automation accelerates materials discovery. *Nat. Mater.* **21**, 722–726.
31. Balandat, M., Karrer, B., Jiang, D.R., Daulton, S., Letham, B., Wilson, A.G., and Bakshy, E. (2019). BoTorch Bayesian optimization in PyTorch. https://botorch.org/tutorials/multi_objective_bo.
32. Osama, M., Shahriari, B., and Schmidt, M. (2016). Do we need “harmless” Bayesian optimization and “first-order” Bayesian optimization? <https://bayesopt.github.io/papers/2016/Ahmed.pdf>.
33. Mirigliano, M., Borghi, F., Podestà, A., Antidormi, A., Colombo, L., and Milani, P. (2019). Non-ohmic behavior and resistive switching of Au cluster-assembled films beyond the percolation threshold. *Nanoscale Adv.* **1**, 3119–3130.
34. Luo, E.Z., Heun, S., Kennedy, M., Wollschläger, J., and Henzler, M. (1994). Surface roughness and conductivity of thin Ag films. *Phys. Rev. B Condens. Matter* **49**, 4858–4865.
35. Muecke, U.P., Messing, G.L., and Gauckler, L.J. (2009). The Leidenfrost effect during spray pyrolysis of nickel oxide-gadolinia doped ceria composite thin films. *Thin Solid Films* **517**, 1515–1521.
36. Luigi 2.8.13 documentation. <https://luigi.readthedocs.io/en/stable/>.